



# Monitoring multi-axial vibrations of flexible rockets using sensor-instrumented reference strain structures



Natsuki Tsushima<sup>a</sup>, Weihua Su<sup>a,\*</sup>, Hector Gutierrez<sup>b</sup>, Michael G. Wolf<sup>c</sup>,  
Edwin D. Griffin<sup>d</sup>, Jarrod T. Whittaker<sup>d</sup>, Marie P. Dumoulin<sup>d</sup>

<sup>a</sup> Department of Aerospace Engineering and Mechanics, University of Alabama, Tuscaloosa, AL 35487-0280, USA

<sup>b</sup> Department of Mechanical and Aerospace Engineering, Florida Institute of Technology, Melbourne, FL 32905, USA

<sup>c</sup> NASA Kennedy Space Center, Kennedy Space Center, FL 32899, USA

<sup>d</sup> a.i. solutions, Inc., Cape Canaveral, FL 32920, USA

## ARTICLE INFO

### Article history:

Received 30 March 2017

Received in revised form 23 June 2017

Accepted 18 September 2017

Available online 21 September 2017

### Keywords:

Reference strain structure

Flexible rocket

Strain sensor

Optimization

Structural dynamics

## ABSTRACT

Strain sensors (e.g., fiber optic strain sensors) can be used to measure the deformation of flexible rockets during launches, in order to monitor and control rocket flight attitude. In this paper, strain sensors are instrumented on multi-axial reference strain structures for a convenient monitor of rocket bending vibrations. Reference strain structures are attached longitudinally along the outer surface of thin-walled flexible rockets. As the medium between the sensors and rocket, the structural design of reference strain structures, as well as the sensor spacing along them, is optimized using an integrated multi-objective optimization approach, which ensures that the reference strain structures will accurately track the deformation of the rocket surface. In addition, kinematic equations are developed to allow for an accurate prediction of the bending deflection of the rocket center axis by using the strain data measured on the rocket surface. Finally, the performance of the optimal reference strain structure is evaluated using different numerical simulations of the flexible rocket.

© 2017 Elsevier Masson SAS. All rights reserved.

## 1. Introduction

In current launch vehicle attitude control systems, inertial measurement units (IMU) are used to measure the rigid-body kinematics of a rocket [1]. The data that IMUs can measure are still limited. In particular, the bending vibration of flexible rockets needs to be accurately monitored and considered in rocket attitude control. Recently, Fiber Optic Strain Sensors (FOSS) based on Fiber Bragg Grating have been used to measure the distributed strain of aerospace structures, such as rocket bodies and flexible aircraft wings [2–4]. One of the advantages of using FOSS arrays for measurement is their capability of providing a reliable sensitivity to strains of mechanical structures [5,6]. Another advantage of FOSS arrays is their small cost in weight. FOSS arrays are lightweight and may be embedded at various locations of a structure without a large weight penalty. Recent applications of FOSS arrays in aerospace structures include direct measurement of structural strains/temperatures or structural health monitoring [2–4,7]. At the same time, with the advent of FOSS array interrogation systems that have a wide bandwidth of more than 1,000 Hz [8], integration of attitude control

systems of flexible rockets with FOSS arrays becomes possible. In such systems, FOSS arrays may not only provide the ability to observe the rocket deformation through strain measurements, but also potentially facilitate the vibration control of the flexible structure using the measured data.

In doing so, a method is needed to improve the bending monitoring along flexible rockets with proper and convenient implementation of the fiber optic strain sensors. Even though there are advantages of applying fiber optic strain sensors for monitoring the bending vibrations of flexible rockets, it becomes obviously inconvenient to directly install the sensors on the rocket surface. To address the convenience of operation and maintenance, an indirect measurement approach can be considered. In this work, a modular design of the reference strain structures (RSS) has been considered. Fiber optic strain sensors are instrumented on the reference strain structures, which are further attached to the rocket surface. Obviously, the concept of reference strain structures is implemented to provide spanwise placement freedom for the sensors. The fiber optic sensors directly measure strains of the reference structures. This measurement is used to indirectly track the real bending/torsional curvatures of the rocket surface. Therefore, in order for this measurement to function reliably and properly, the placement of reference structures and fiber optic sensors needs to be properly

\* Corresponding author.

E-mail address: suw@eng.ua.edu (W. Su).

## Nomenclature

$A$	Cross-sectional area of rocket	$\text{m}^2$	$\varepsilon_0$	Measured strain from 0-degree oriented sensor
$\mathbf{A}_u, \mathbf{A}_v$	Coefficient matrices of shifted Legendre polynomials		$\varepsilon_{45}$	Measured strain from 45-degree oriented sensor
$b$	Width of RSS beam	$\text{m}$	$\varepsilon_{axial}$	Axial strain, from FE simulation
$d$	Uniform sensor spacing on each RSS beam	$\text{m}$	$\varepsilon_{BX}$	Bending strain about the x axis, processed from sensor measurement
$E$	Young's modulus	$\text{GPa}$	$\varepsilon_{BY}$	Bending strain about the y axis, processed from sensor measurement
$f_i$	Optimization objective function		$\varepsilon_S$	Shear strain of each RSS beam, processed from sensor measurement
$G$	Shear modulus	$\text{GPa}$	$\varepsilon_{xy}$	Shear strain, from FE simulation
$h$	Thickness of RSS beam	$\text{m}$	$\varepsilon_s^{ref}$	Average shear strain of RSS beams
$I$	Moment of inertia	$\text{m}^4$	$\varepsilon_0^{ref}$	Axial strain of rocket reference axis (positive compressive)
$l$	Longitudinal linkage spacing between RSS beams and rocket	$\text{m}$	$\eta$	Modal coordinate
$n_{sensor}$	Number of sensors on each RSS beam		$\theta$	Angular spacing between each RSS beam
$\mathbf{P}$	Shifted Legendre polynomials		$\kappa_x, \kappa_y, \kappa_z$	Bending curvatures about the x and y axes and twist curvature about the z axis
$p$	Order of Legendre polynomials		$\nu$	Poisson's ratio
$r$	Radial linkage spacing between RSS beams and rocket	$\text{m}$	$\rho$	Material density
$S_{BX}, S_{BY}, S_\theta$	Bending and torsional sensitivities		$\varphi$	Linear mode shape
$u$	Bending deflection in the x direction	$\text{m}$	$\omega$	Natural frequency
$v$	Bending deflection in the y direction	$\text{m}$		$\text{Hz}$
$x_d$	Design variable for RSS design optimization			
$x_s$	Design variable for sensor placement optimization			

designed and optimized to ensure precise vibration monitoring with the sensor measurements.

Even though studies of accurate and efficient strain/temperature sensing and structural health monitoring with fiber optic strain sensors have been performed [2–7], a reliable method to incorporate such sensors for the application of shape or vibration monitoring of aerospace structures has not been fully explored. Therefore, it is opportune to study and prove the feasibility of FOSS for vibration monitoring applications. In a previous study, a real-time beam bending solution [9] was developed by Su et al. to obtain the instantaneous beam kinematics based on the measurement data from discontinuous FOSS along the beam and a single IMU. Additionally, an algorithm was developed to decouple the combined strain information measured by the FOSS on a beam structure into extensional strain, twist curvature, and bending curvatures [10]. By combining this with the real-time beam bending solution, it enables one to predict deflections of the flexible rocket along the center axis based on the measured strains on the rocket surface.

Since previous studies regarding real-time simulation and control system development using FOSS [8,9] have focused on a scaled beam model, this paper explores how such strain sensors work with full-size flexible rockets using the concept of reference strain structures. While most of the studies involved in this paper will be applicable to other types of sensors, FOSS are considered to be applied for the strain measurement of flexible rockets. To carry out these studies, a full-size flexible rocket with modular reference strain structures will be modeled as a platform for further structural dynamic and control studies. Based on the finite-element model, the first objective of this study is to design and optimize the reference strain structures, with the intent of accurately observing bending deformations of flexible rockets through indirect measurement. Although the main target of the strain sensor instrumented on RSS is to provide an accurate bending vibration monitoring of the flexible rocket, it is also capable of observing the torsional deformation. Second, the feasibility of the optimal reference strain structure will be demonstrated by evaluating its ability to capture the strain of a flexible rocket. Third, several parameters (such as the sensor placement on the RSS) involved in the prediction of the bending deformations will be optimized to obtain the most accurate estimations out of the RSS-sensor system. Last,

**Table 1**

Wall thickness of each section of the notional rocket.

Rocket section	Thickness (m)
Fairing	0.015
Payload	0.005
Centaur tanks	0.012
ISA	0.005
Oxygen tank	0.005
Fuel tank	0.005
Booster and sustainer	0.01

transient simulations of the flexible rocket will be performed to evaluate the performance of the optimum reference structure with properly instrumented strain sensors, in terms of the accuracy of its prediction of the bending deflections of the rocket center axis.

## 2. Structural analysis model

In the structural analysis of the current study, a finite-element (FE) model of a notional flexible rocket with multi-axial RSS beams is created in MSC.Patran, based on the published information of the Atlas Centaur Surveyor launch vehicle [11]. Fig. 1 shows the breakdown of the rocket sections. The geometric and material properties are obtained from Ref. [11] and additional reports [12, 13]. The rocket model has two main components: the conical fairing and the remaining cylindrical body. CQUAD4 shell elements are used to mesh the cylindrical surface of the rocket model, with 640 and 72 elements in the longitudinal and circumferential directions, respectively. Weight and rigidity distributions of the shell elements are referred to the data in Ref. [11], with all tanks being empty. However, the properties are uniform in each section for simplicity, as shown in Figs. 2 and 3. The thickness of the shell elements in each section is assigned according to Table 1. The Poisson's ratio  $\nu = 0.33$  is used for the materials of all sections. Internal tank pressures are applied on oxygen/fuel tanks and the Centaur tank in the following studies, where the values of the pressure are obtained from the lift-off testing described in Ref. [11].

As shown in Fig. 4, an array of three RSS beams is attached to the outer surface of the rocket along the longitudinal direction through rigid links, which separate from each other by  $120^\circ$  along

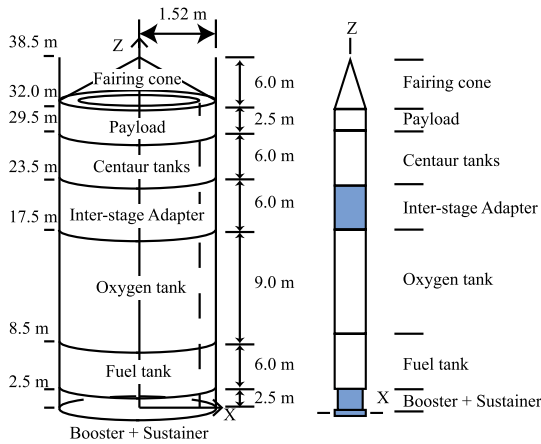


Fig. 1. The flexible rocket model components.

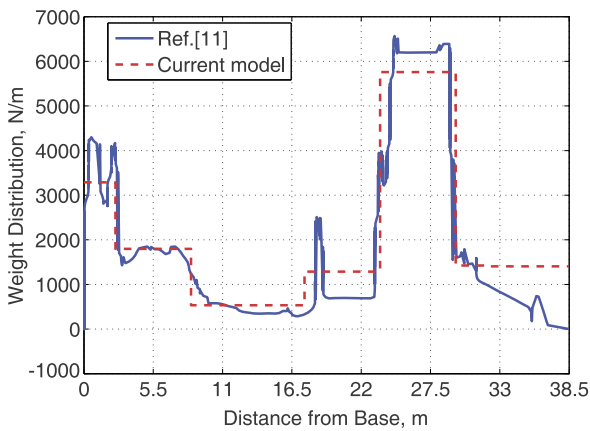


Fig. 2. Rocket weight distribution.

the circumferential direction of the rocket body. The RSS beams run through the entire span of the rocket, excluding the conical faring. These beams are uniform with a rectangular cross-section, even though other cross-sectional shapes may be further designed. Strain sensors are instrumented on the RSS beams, which indirectly monitor the deformation of the rocket surface if the RSS beams and strain sensors are well designed and distributed. For the current study, five design parameters are selected, which are the longitudinal spacing  $l$  of the links connecting the rocket and RSS, the radial spacing  $r$  of the links

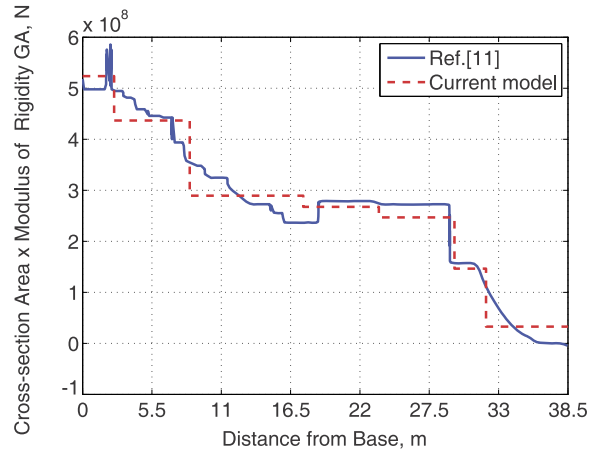
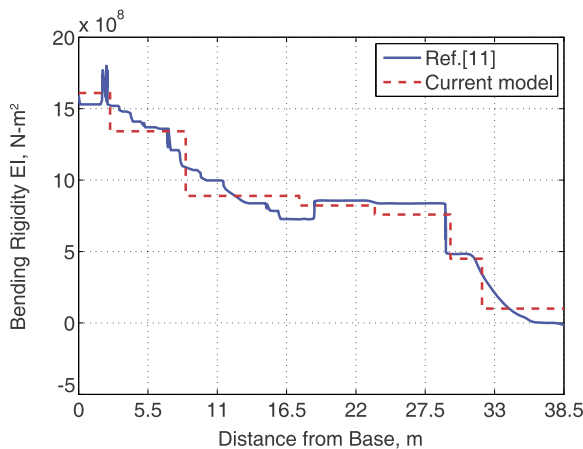


Fig. 3. Rocket rigidity property distributions.

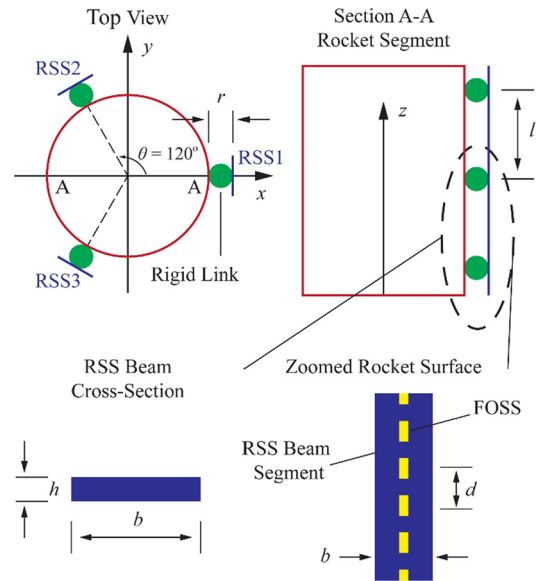


Fig. 4. Multi-axial RSS design concept.

between the rocket and RSS, the RSS beam thickness  $h$ , the RSS beam width  $b$ , and the sensor spacing  $d$  along the RSS (see Fig. 4). Three RSS beams are needed to measure multi-axial bending and torsional deformations of the rocket. The first RSS (RSS1) is located on the rocket surface along the  $z$  direction (defined as  $\theta = 0^\circ$ ), and the second (RSS2) and the third (RSS3) are located at  $\theta = 120^\circ$  and  $240^\circ$ , respectively, as shown in Fig. 4. The initial beam thickness is  $h = 3.18$  mm and the width is  $b = 12.7$  mm. The material properties of the RSS beams are Young's modulus  $E = 70$  GPa, shear modulus  $G = 26$  GPa, and Poisson's ratio  $\nu = 0.33$ . CQUAD4 shell elements are also used to mesh the RSS beams, with 640 and 2 elements in the spanwise (longitudinal) and width directions, respectively. The side nodes along the RSS beams are rigidly linked to the rocket surface using RBE2 elements, as shown in Fig. 5.

### 3. Theoretical formulation

This section discusses kinematic equations to estimate the bending deflection of a flexible rocket along its center axis by using the measured strains from RSS beams. Furthermore, optimizations of the RSS-sensor configuration are introduced to obtain the most accurate estimation of the system.

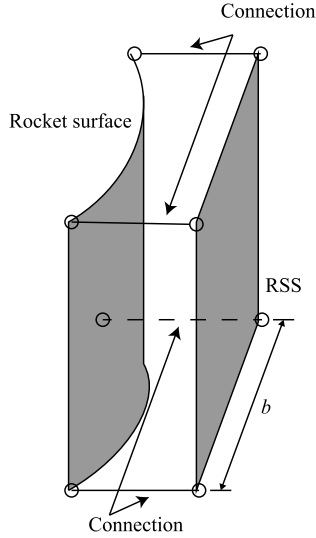


Fig. 5. Link configuration between rocket surface and RSS beam.

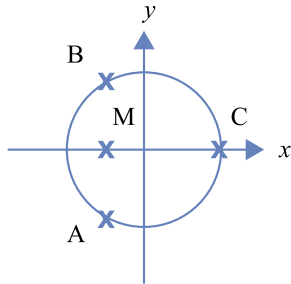


Fig. 6. Circumferential positions of three RSS beams around the rocket (top view).

### 3.1. Kinematic equations

From the previous discussion, the RSS beams serve as the medium between the rocket and strain sensors. Even if the indirect measurement of rocket deformation through the RSS beams is accurate, a kinematic relation is still needed, such that the deflection of the rocket center axis may be derived from the strains of the rocket surface measured by the sensors. The kinematics are also helpful in the further development of real-time control algorithms for the rocket. The kinematics involve two steps of calculation. The first is to derive the bending/torsional curvatures of the rocket center axis from the measured strain data, following the approach developed in Ref. [10]. The discontinuous curvatures along the rocket center axis are further used to approximate the deflection at any location along the axis [9].

#### 3.1.1. Estimation of rocket bending curvatures

The kinematic equations derived in Ref. [10] are applied to obtain the bending curvatures of the rocket center axis about the  $x$  and  $y$  directions according to the strains measured at the three RSS beams. This method was originally derived to take input strains from three surfaces of a boxed beam [10], which is modified to accommodate three RSS beams with a  $120^\circ$  angular spacing around the rocket circumference. Fig. 6 shows the circumferential positions of the three RSS beams around the rocket. RSS C (the same as RSS1 in Fig. 4) is located at  $0^\circ$  from the  $x$  axis, while RSS B and A are  $120^\circ$  from each other in the counter-clockwise direction. Strain sensors are placed on the three RSS beams at alternating  $0^\circ$  and  $45^\circ$  orientations (Fig. 7). An initial data processing is performed to interpolate the strain data measured by  $0^\circ$ -sensors, in order to compensate for the unavailable measurement data where sensors

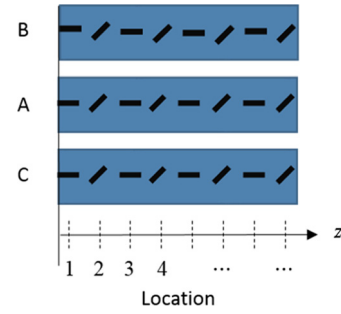


Fig. 7. Sensors placement with alternating orientations.

are placed at  $45^\circ$  as well as additional desired locations. For example, the sensor placed at location 2 in Fig. 7 is orientated along  $45^\circ$ . In order to obtain the strain along  $0^\circ$  at this location, one has to interpolate the measurement data at locations 1 and 3, where the corresponding sensors are both orientated along  $0^\circ$ . The same procedure is used to process the strain data of  $45^\circ$ -sensors.

The interpolated strain data of  $0^\circ$  and  $45^\circ$  at a given longitudinal location are denoted as  $\varepsilon_0$  and  $\varepsilon_{45}$ , respectively, which determine the shear strain

$$\varepsilon_s = \varepsilon_{45} - \frac{1-\nu}{2} \varepsilon_0 \quad (1)$$

The shear strain of the rocket center axis at that longitudinal location is obtained by averaging the data of three RSS beams, i.e.,

$$\varepsilon_s^{ref} = \frac{1}{3} (\varepsilon_s^A + \varepsilon_s^B + \varepsilon_s^C) \quad (2)$$

Similarly, the normal strain (positive compressive)  $\varepsilon_0^{ref}$  of the reference axis is

$$\varepsilon_0^{ref} = \frac{\varepsilon_0^M - \varepsilon_0^C \cos \theta}{1 - \cos \theta}, \quad (3)$$

$$\varepsilon_0^M = \frac{1}{2} (\varepsilon_0^A + \varepsilon_0^B)$$

where  $\varepsilon_0^M$  is the normal strain at point M as the middle between A and B (see Fig. 6), which is right on the  $x$  axis. Strains related to bending in the  $x$  and  $y$  axes are

$$\begin{aligned} \varepsilon_{BY} &= \varepsilon_0^{ref} - \varepsilon_0^C, \\ \varepsilon_{BX} &= \varepsilon_0^B - \varepsilon_0^M \end{aligned} \quad (4)$$

Finally, the curvatures of the rocket center axis about each direction can be obtained by multiplying the corresponding sensitivities  $S_{BX}$ ,  $S_{BY}$ , and  $S_\theta$ , given as

$$\kappa_x = \frac{\varepsilon_{BX}}{S_{BX}}, \quad \kappa_y = \frac{\varepsilon_{BY}}{S_{BY}}, \quad \kappa_z = \frac{\varepsilon_s^{ref}}{S_\theta} \quad (5)$$

These sensitivities consist of structural properties of the rocket and dominant deformation modes (especially in dynamic cases). It is convenient to calibrate them from experiments or FE analysis in case of very complicated structures such as rockets by observing both the strains and curvatures.

#### 3.1.2. Deflection of rocket center axis

The bending curvatures along the rocket center axis were derived in the previous section, which were based on discontinuous data corresponding to where the interpolation was performed. A further calculation is performed to recover the bending deflection at any location along the center axis from these discontinuous curvature data using the method introduced in Ref. [9]. At any time, the bending deflection of the rocket can be expressed as the

combination of its linear normal modes weighted by their magnitudes, which is

$$\begin{aligned} \mathbf{u}(z, t) &= \sum_{j=1}^{\infty} \varphi_{uj}(z) \eta_{uj}(t) = \Phi_{\mathbf{u}} \boldsymbol{\eta}_{\mathbf{u}}, \\ \mathbf{v}(z, t) &= \sum_{j=1}^{\infty} \varphi_{vj}(z) \eta_{vj}(t) = \Phi_{\mathbf{v}} \boldsymbol{\eta}_{\mathbf{v}} \end{aligned} \quad (6)$$

where  $\mathbf{u}$  and  $\mathbf{v}$  are the bending deflections in the  $x$  and  $y$  directions,  $\Phi_{\mathbf{u}}$  and  $\Phi_{\mathbf{v}}$  are the linear bending normal modes of the rocket in the  $x$  and  $y$  directions, and  $\boldsymbol{\eta}_{\mathbf{u}}$  and  $\boldsymbol{\eta}_{\mathbf{v}}$  are the corresponding modal coordinates. The modes are calculated from a finite-element analysis of the full rocket model, with the modal information of the center axis extracted. Obviously, the modes are all discrete. In order to obtain the deflections at any point along the center axis, one can use the shifted Legendre polynomials to approximate the discrete modes [9], given as

$$\begin{aligned} \Phi_{\mathbf{u}}(z_0) &= \mathbf{P}(z_0) \mathbf{A}_{\mathbf{u}}, \\ \Phi_{\mathbf{v}}(z_0) &= \mathbf{P}(z_0) \mathbf{A}_{\mathbf{v}} \end{aligned} \quad (7)$$

where  $z_0$  are the discrete locations accounted in the center line bending modes.  $\mathbf{P}$  is a matrix consisting of column vectors of individual shifted Legendre polynomials evaluated at  $z_0$  [9], while the number of involved polynomials (i.e., number of columns for  $\mathbf{P}$ ) is yet to be further determined. As the mode shapes and values of Legendre polynomials are all known, the coefficient matrices  $\mathbf{A}_{\mathbf{u}}$  and  $\mathbf{A}_{\mathbf{v}}$  are obtained by

$$\begin{aligned} \mathbf{A}_{\mathbf{u}} &= \mathbf{P}(z_0)^{-1} \Phi_{\mathbf{u}}(z_0), \\ \mathbf{A}_{\mathbf{v}} &= \mathbf{P}(z_0)^{-1} \Phi_{\mathbf{v}}(z_0) \end{aligned} \quad (8)$$

Note that the  $\mathbf{P}$  matrix is generally not invertible. Therefore, the Moore–Penrose pseudo-inverse method is used in the calculation. Finally, with the approximated mode shapes, the nodal displacements can be expressed as

$$\begin{aligned} \mathbf{u}(z, t) &= \mathbf{P}(z) \mathbf{A}_{\mathbf{u}} \boldsymbol{\eta}_{\mathbf{u}}(t), \\ \mathbf{v}(z, t) &= \mathbf{P}(z) \mathbf{A}_{\mathbf{v}} \boldsymbol{\eta}_{\mathbf{v}}(t) \end{aligned} \quad (9)$$

With known bending curvatures, one may solve for the modal coordinate magnitudes using derivatives of the Legendre polynomials, such that

$$\begin{aligned} \eta_{\mathbf{u}}(t) &= (\mathbf{P}''(z) \mathbf{A}_{\mathbf{u}})^{-1} \boldsymbol{\kappa}_{\mathbf{y}}(z, t), \\ \eta_{\mathbf{v}}(t) &= (\mathbf{P}''(z) \mathbf{A}_{\mathbf{v}})^{-1} \boldsymbol{\kappa}_{\mathbf{x}}(z, t) \end{aligned} \quad (10)$$

The approach avoids the spatial integration of the bending curvatures in order to obtain the bending deflections of the rocket center axis.

### 3.2. Optimization of RSS structure and placement of strain sensors

The kinematic equations assume that the sensors can accurately measure the strains of the rocket surface. As discussed previously, RSS beams are used as the medium to install the sensors. Therefore, the RSS beams and sensor placement on them need to be optimized to achieve the most accurate estimation of the rocket deformation. The whole optimization of RSS-sensor structures includes two sub-problems. The first is the structural design optimization of the RSS beams and the other is to optimize the sensor spacing along the RSS beams.

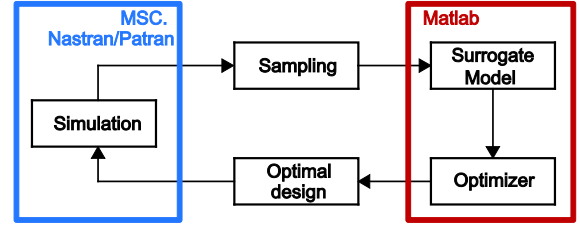


Fig. 8. Surrogate-based structural optimization for RSS beams.

#### 3.2.1. Optimization of RSS structural design

The objective of this optimization is to minimize the strain difference between the rocket surface and RSS beams, so that the rocket deformation is accurately measured by the sensors instrumented on the RSS beams. The performance of the RSS beams depends on their dimensions and the spacing of the linkage between the rocket and RSS beams in both radial and longitudinal directions (see Fig. 4). Therefore, the two objective functions of the optimization are the root mean square (RMS) axial and shear strain differences between the rocket and RSS beams. Furthermore, attaching RSS beams to the rocket also introduces a weight penalty, which should be minimized as well. The RSS structural optimization problem is defined as

$$\begin{aligned} \min_{x_d} f_1(x_d) &= \sqrt{\frac{1}{N} \sum_{n=1}^N (\varepsilon_{axial}^{rocket} - \varepsilon_{axial}^{RSS})^2}, \\ \min_{x_d} f_2(x_d) &= \sqrt{\frac{1}{N} \sum_{n=1}^N (\varepsilon_{xy}^{rocket} - \varepsilon_{xy}^{RSS})^2}, \\ \min_{x_d} f_3(x_d) &= \rho h b \end{aligned} \quad (11)$$

where the superscript “rocket” indicates the strain values of the rocket surface and “RSS” denotes the strain values for the corresponding RSS beams, and  $\varepsilon_{axial}$  and  $\varepsilon_{xy}$  are the axial and shear strains, obtained from the FE analysis. The design variable  $x_d = \{l, r, h, b\}^T$ , includes the linkage spacing in the longitudinal direction  $l$ , the radial spacing  $r$ , RSS beam cross-sectional thickness  $h$ , and cross-sectional width  $b$ . The design constraints are

$$\begin{aligned} 0.05 \text{ m} &\leq l \leq 0.25 \text{ m}, \\ 0.005 \text{ m} &\leq r \leq 0.1 \text{ m}, \\ 0.003 \text{ m} &\leq h \leq 0.01 \text{ m}, \\ 0.01 \text{ m} &\leq b \leq 0.05 \text{ m}, \\ \omega_{rocket} &< \omega_{RSS} \end{aligned} \quad (12)$$

where  $\omega_{rocket}$  are the natural frequencies of the notional rocket model and  $\omega_{RSS}$  are the natural frequencies of the RSS beams. The last constraint is to separate the natural frequencies of the rocket and RSS beams, so that the RSS beams are not excited by the vibration of the rocket. The upper limit of the longitudinal spacing 0.25 m gives a reasonable natural frequency range of the RSS beams. The optimization problem is solved with the fast elitist nondominated sorting genetic algorithm (NSGA-II) [14]. To accelerate the optimization process, a surrogate model is constructed using the Kriging method [15] with a finite number of sampling data based on the simulation results from MSC.Nastran.

The optimization process is depicted in Fig. 8. The whole process consists of 1) developing the FE model in MSC.Patran, 2) collecting sampling data from the FE analysis in MSC.Nastran, 3) constructing the surrogate model using the Kriging method with the sampling data, 4) finding the optimal RSS structural design with the NSGA-II algorithm, and 5) performing the FE analysis using the optimal design to evaluate the objective functions.

### 3.2.2. Optimization of stain sensor placement

With the RSS structural design converged to the optimum, it is still necessary to properly determine the number of strain sensors to be instrumented along RSS beams. As the kinematic equations presented in the previous section interpolate the measured strain data to calculate the bending/torsional curvatures of the rocket center axis, the choice of strain sensor spacing (i.e., the number of sensors on a RSS beam) influences the accuracy of the interpolation and the estimated bending/torsional curvatures. Therefore, one has to minimize the following objective functions of

$$\begin{aligned} \min_{x_s} f_4(x_s) &= \sqrt{\frac{1}{N} \sum_{n=1}^N (\kappa_x^{FEM} - \kappa_x^{EST})^2}, \\ \min_{x_s} f_5(x_s) &= \sqrt{\frac{1}{N} \sum_{n=1}^N (\kappa_y^{FEM} - \kappa_y^{EST})^2}, \\ \min_{x_s} f_6(x_s) &= \sqrt{\frac{1}{N} \sum_{n=1}^N (\kappa_z^{FEM} - \kappa_z^{EST})^2}, \\ \min_{x_s} f_7(x_s) &= n_{sensor} \end{aligned} \quad (13)$$

where the superscript “FEM” indicates rocket center axis curvature values directly derived from the FE simulation using MSC.Nastran, while “EST” denotes the curvatures estimated by the measured strain data from RSS. Quantity  $n_{sensor}$  is the number of sensors used on an RSS beam. If the sensors are evenly placed, the sensor spacing  $x_s$  is a discrete value selected from the following set of

$$x_s = [0.4, 0.5, 0.8, 1.0, 1.6, 2.0] \text{ m} \quad (14)$$

The spacing variables in the set give 16 to 80 sensors on each RSS beam, where the maximum number of sensors is determined by the capability of the data processing equipment.

The problem involves a discrete design variable, whose dimension is not large. Without applying a sophisticated optimization scheme, several FE simulations are performed to traverse all the possible design variables in the design space. The optimum solution is found after the enumerating process.

## 4. Numerical studies

In this section, numerical studies are presented to optimize the RSS beams. In addition, finite-element simulations of the flexible rocket with the optimum RSS beams are performed to demonstrate the feasibility of the concept using reference stain structures instrumented with strain sensors to monitor the vibrations of flexible rockets.

### 4.1. Modal characteristics of notional rocket and RSS model

A modal analysis is performed to make sure that the modal characteristics of the rocket FE model are comparable to the experimental data in Ref. [11]. Fig. 9 shows the first two bending mode shapes of the rocket model. Natural frequencies of the first three bending modes from the modal analysis are compared with those of the reference rocket measured in experiments [11] as shown in Table 2. Free-free boundary conditions are applied in both the modal analysis and the experiments. Note that the natural frequencies of the reference rocket were measured when the tanks were partially pressurized, which is not captured in the current model. Therefore, it is reasonable that the natural frequencies of the reference rocket are slightly higher than the results of the current model. However, the natural frequencies of the current model

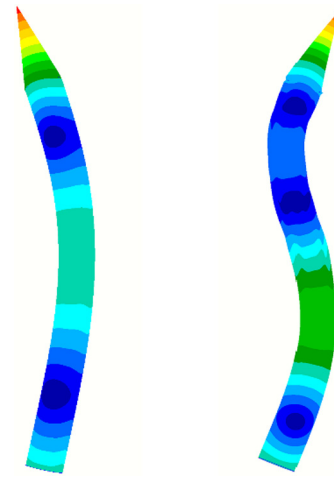


Fig. 9. The first (left) and second (right) bending mode shapes.

Table 2

Natural frequencies of the current model and reference rocket.

Bending mode	Direction	Simulated (Hz)	Experiment (Hz)
1	y-z plane	6.05	6.12
	x-z plane	6.05	6.21
2	y-z plane	14.61	14.51
	x-z plane	14.61	13.49
3	y-z plane	24.90	31.90
	x-z plane	24.90	31.40

Table 3

Change of the first natural frequency of RSS with longitudinal linkage spacing.

Axial spacing $l$ (m)	Frequency (Hz)
0.1	1516.2
0.25	234.86
0.5	65.345

are in the expected range for the study. In addition, the natural frequencies of RSS beams should be out of the range of the frequencies of both the rocket and the control system (0 to 200 Hz). Table 3 shows the lowest natural frequencies of the RSS beams with the change of the longitudinal spacing of the linkage that connects the RSS beams and the rocket. According to Tables 2 and 3, it is preferred to constrain the longitudinal spacing of the RSS-rocket linkage to be less than 0.25 m, so that the natural frequencies of the RSS beams do not interfere with those of the rocket.

### 4.2. Optimization of RSS beam structure

For optimization studies of RSS beams, the baseline RSS beams are defined with the thickness and width of  $h = 0.00318$  m and  $b = 0.0127$  m, respectively. The three RSS beams are connected to the flexible rocket surface with rigid links, with the initial longitudinal and radial spacing of  $l = 0.05$  m and  $r = 0.015$  m, respectively. The rocket is cantilevered at its root, while tip loads of 1 kN are applied in both the x and y directions. An additional torque of 1094.4 kN-m about the z axis is also applied. The fuel tank pressure is 405 kPa and the oxygen tank pressure is 212.5 kPa. The Centaur tank is pressurized at 103 kPa. Note that even though a complex load of both bending and torsion is applied, the target of the study is to optimize the RSS beams so as to accurately monitor the bending deformation of the rocket using the measured sensor data. Fig. 10 shows the differences of axial and shear strains between the baseline RSS1 and the connected rocket surface along the RSS1. Results of RSS2 and RSS3 are omitted, since they are

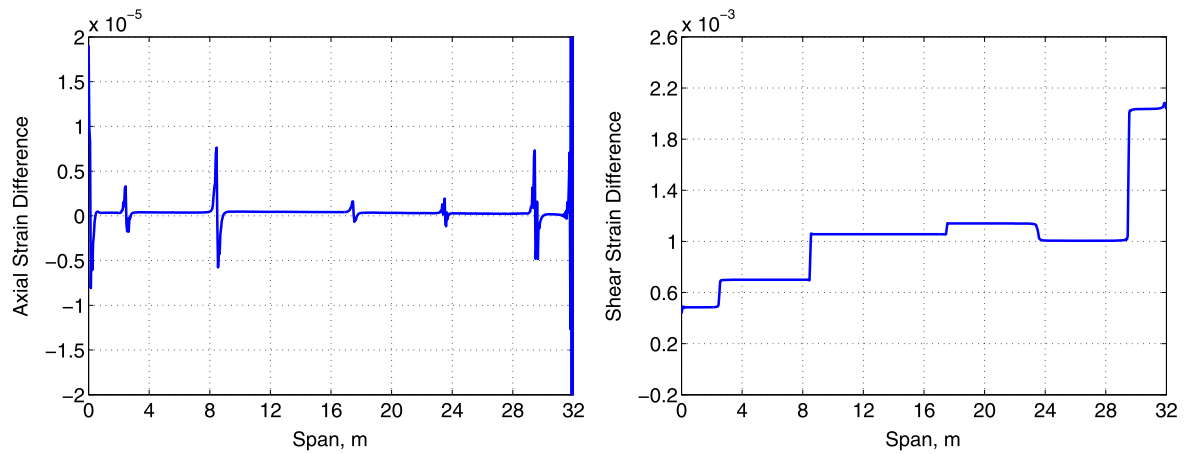


Fig. 10. Differences of axial and shear strains between the baseline RSS1 and the rocket surface with the static loads.

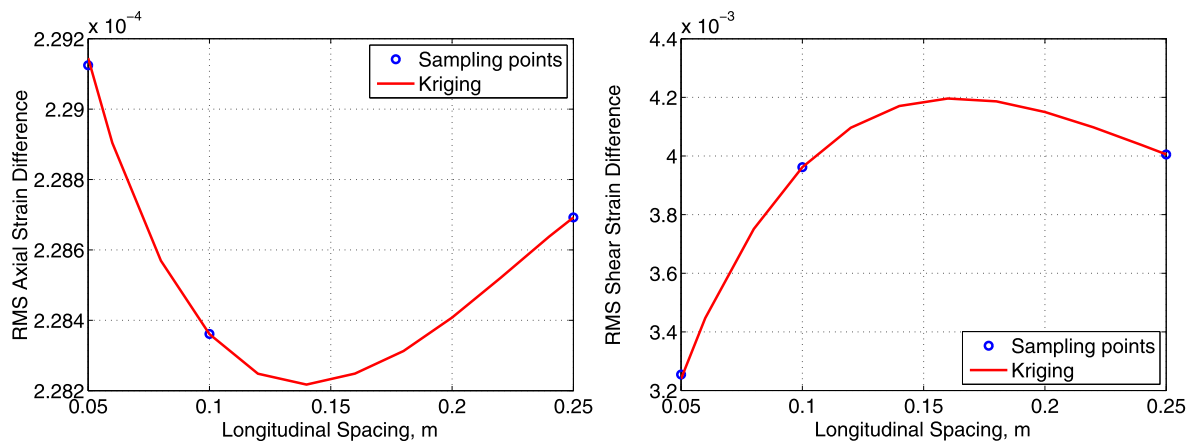


Fig. 11. RMS axial and shear strain differences with different longitudinal spacings.

very similar to those of RSS1. Because of the thickness discontinuity between different rocket sections, relatively large axial strain differences are observed at boundaries between every two sections. The shear strain difference grows one order larger at the top. These differences can be reduced with properly designed RSS beams and sensor placement.

Some statements about the boundary condition used in the current study are provided here. All simulation cases provided in this paper use the cantilever boundary condition at the root of the rocket. While this is not the case in a real rocket flight, it has been used in rocket ground vibration tests. In addition, the purpose of this paper is to explore and demonstrate the concept of using RSS to track the lateral bending vibration of flexible rockets, which can be easily excited and simulated with a cantilever boundary condition and applied loads at the tip. However, the methodology developed in this paper to design and analyze rocket-RSS structures does not exclude the free-free flight conditions for rockets.

The integrated multi-objective optimization is performed to find the optimal RSS dimensions and linkage spacing between the rocket and RSS beams. The Kriging-based surrogate model is firstly constructed using samplings based on FE analyses in MSC.Nastran. Figs. 11–14 show the fitted curves of the RMS axial and shear strain differences with respect to each RSS structural design variable.

The optimum structural design of the RSS beams is found by using the fitted curves. The surrogate-based optimization provides the Pareto optimal choices as shown in Fig. 15. By placing the priority on minimizing the axial strain difference between the

rocket and RSS beams, the optimal design is chosen as  $l = 0.05$  m,  $r = 0.005$  m,  $h = 0.005$  m, and  $b = 0.05$  m, which corresponds to the cross in Fig. 15. The cross-sectional weight of each RSS beam after the optimization is 0.675 kg/m.

A static analysis is performed with the optimum RSS design to evaluate its performance. The applied load and tank pressure are the same as the case with the initial design. Fig. 16 shows the actual axial and shear strains on the rocket surface and the optimal RSS1 beam with the applied static loads, while their differences are plotted in Fig. 17. As a check, the performance of the optimum RSS beam design with a further reduced radial link spacing  $r = 0.001$  m, is also illustrated in Fig. 17, which apparently provides a further reduction of the shear strain difference between the rocket and RSS beam. However, this design is out of the design space as it violates the geometrical constraints considering the thickness of the RSS beams. Additional clearance is also required to install the sensors and to avoid a contact between the RSS beams and the rocket surface. Therefore, the design with  $r = 0.005$  m is used in the following studies. By comparing the current results with those from Fig. 10, it is evident that the performance of the optimized RSS beams is significantly improved with much lower strain differences between the RSS beams and rocket surface.

#### 4.3. Optimization of sensor spacing on RSS beams

Determining the optimal sensor spacing along the RSS beams is the objective of this section. The loading condition is the same as the previous optimization cases. Figs. 18 and 19 plot the RMS curvature differences (as defined in Eq. (13)) with respect to the

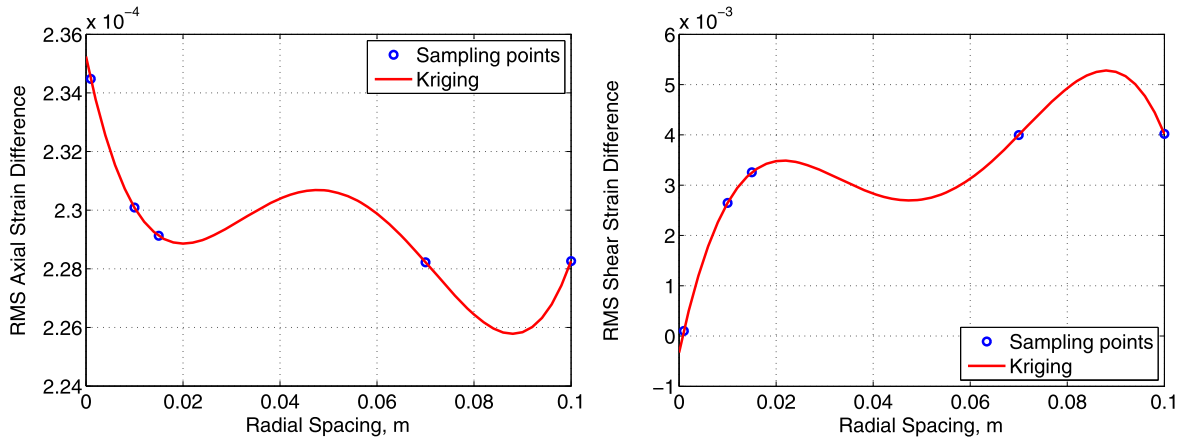


Fig. 12. RMS axial and shear strain differences with different radial spacings.

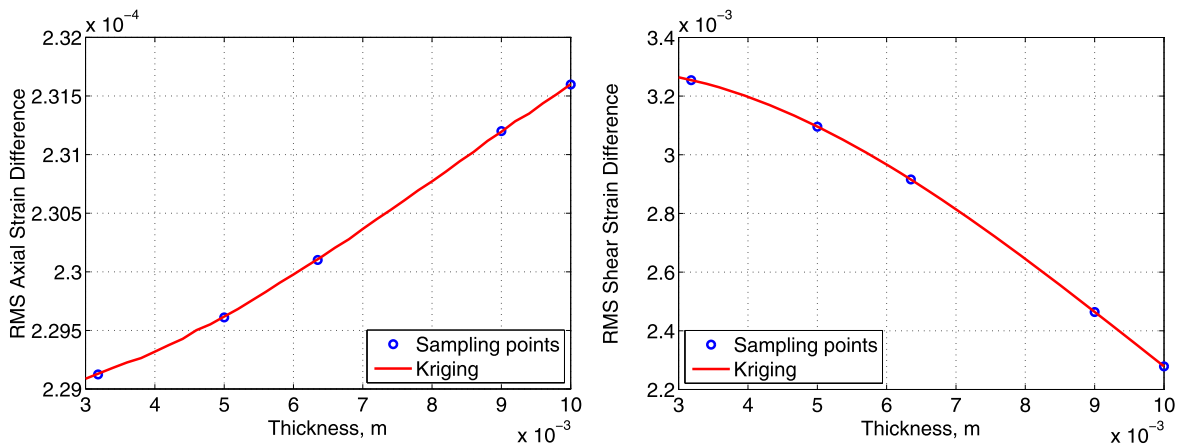


Fig. 13. RMS axial and shear strain differences with different RSS beam thicknesses.

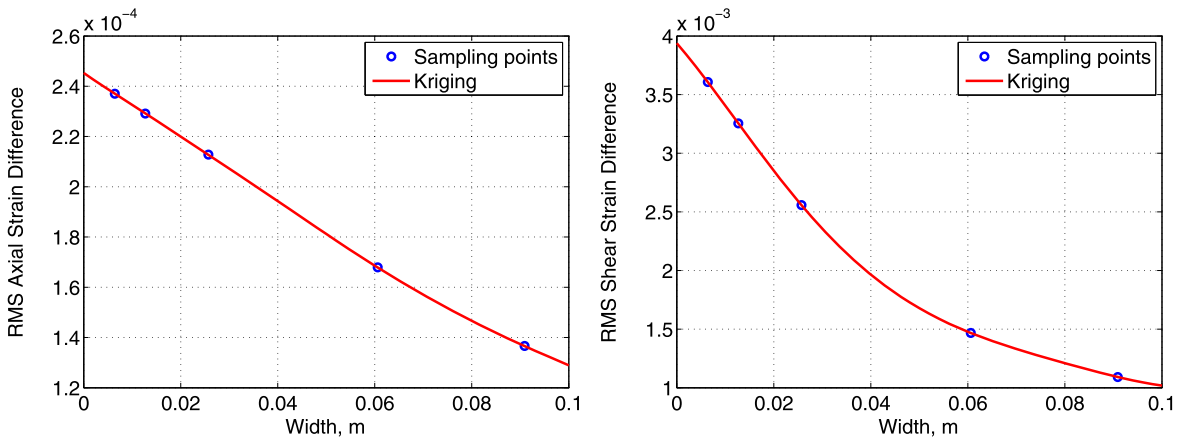


Fig. 14. RMS axial and shear strain differences with different RSS beam widths.

different sensor spacing. Since the sensitivities are well-calibrated for each variable, the estimations are pretty accurate in each case. Eventually, the sensor spacing is selected as 1.6 m by considering the balance of the accuracy of estimations and the number of sensors. In this case, the number of sensors to be installed on each RSS beam is 20. Figs. 20 and 21 highlight the agreement between the bending curvatures of the rocket center axis, obtained directly from the FE analysis and the estimation using the sensor measurement data, respectively.

#### 4.4. Selection of Legendre polynomials

Finally, the order of Legendre polynomials is determined with the optimum RSS design. This ensures an accurate prediction of the bending deflection at any location along the rocket center axis based on the discontinuous curvature data derived from the sensor measurement. The approach described in Eq. (9) is essentially to use the Legendre polynomials to fit the discrete mode shapes, so as to obtain continuous functions of mode shapes. As discussed in Ref. [9], this approach may create large fitting errors on both

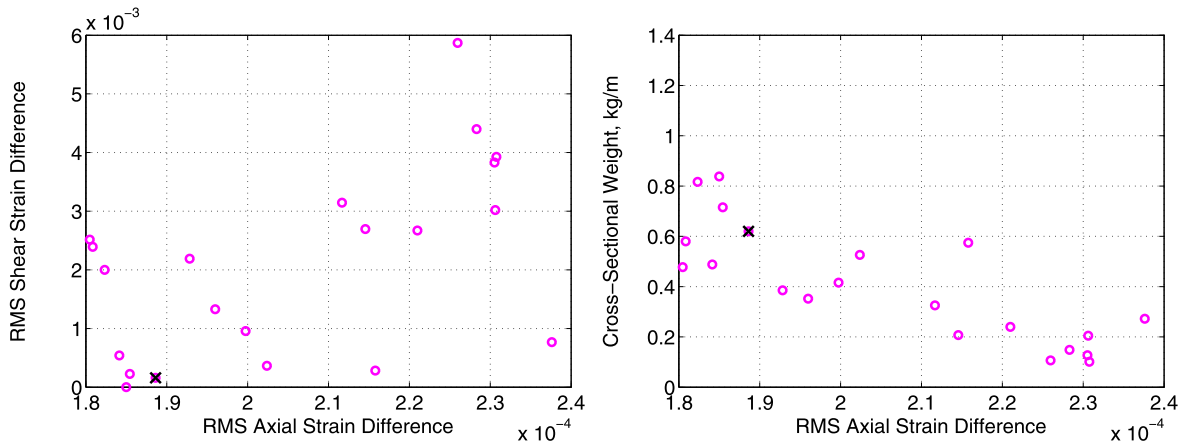


Fig. 15. Pareto-fronts of the RSS design optimization.

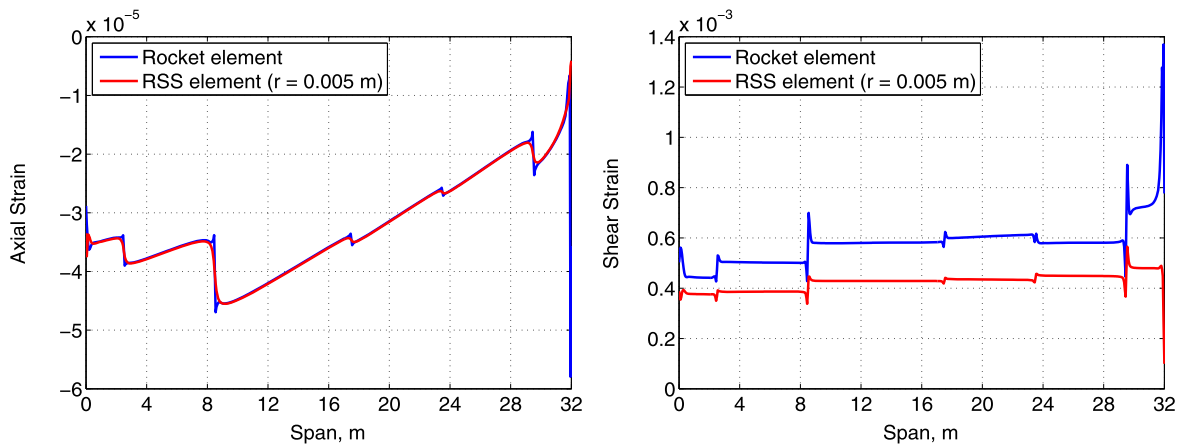


Fig. 16. Axial and shear strains on the rocket surface and the optimal RSS1 with the static loads.

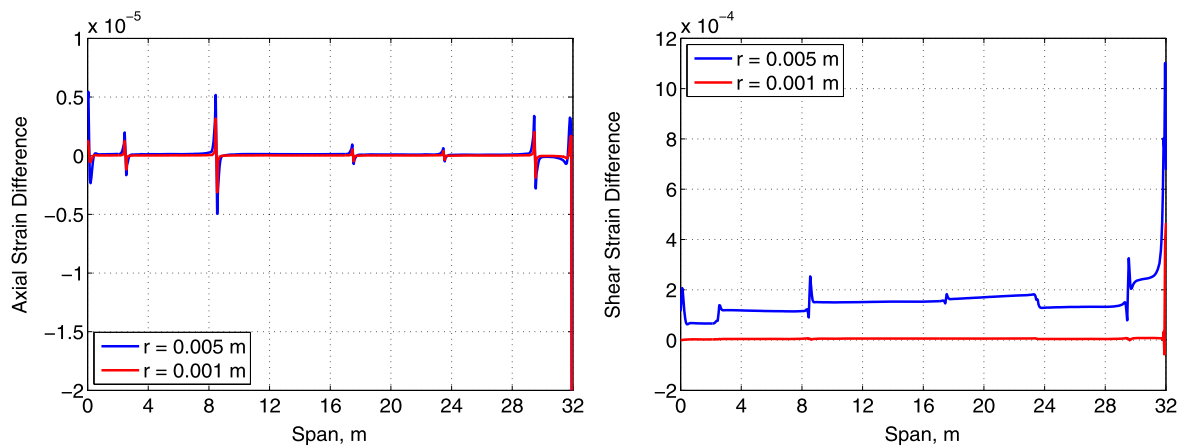


Fig. 17. Axial and shear strain differences on the rocket surface and the optimal RSS1 with the static loads.

ends of the domain (root and tip of the rocket in this study), if the available discrete points representing the modes and the number of Legendre polynomials do not properly match. To ensure the accuracy, a parametric study was carried out to calculate the rocket bending deflection using a varying number of the Legendre polynomials. The results are compared to the FE solution. For good convergence and robustness for the following transient studies, the polynomials up to the 22nd order are used although the first 9 polynomials provide the most accurate estimation with the static loading case. The 22 polynomials with interpolated strain data on

each RSS beam can provide accurate estimations of the bending deflections as shown in Fig. 22.

#### 4.5. Performance evaluation

The optimum design of RSS beams and sensor spacing were found based on static simulations. Therefore, it is necessary to ensure that the optimum design can properly estimate transient bending deflections of the flexible rocket. To understand transient responses of the rocket-RSS system, a frequency analysis is per-

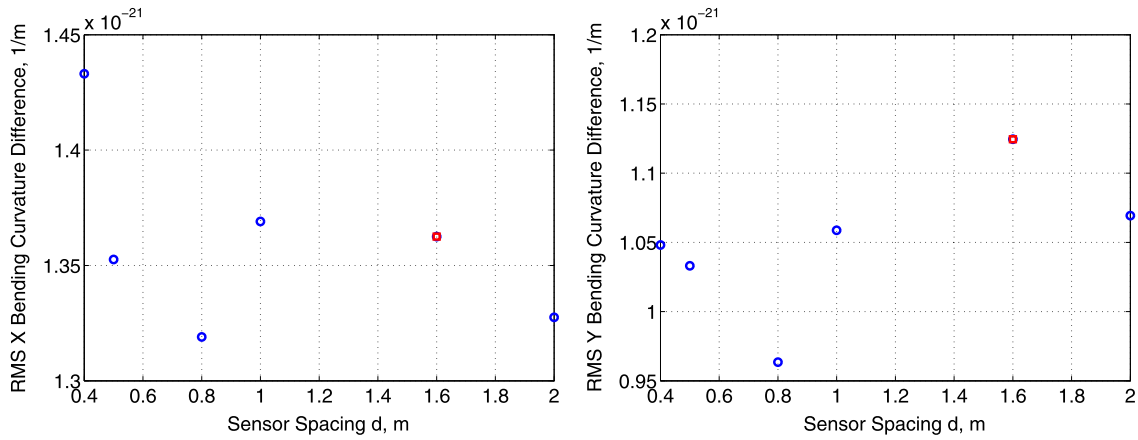


Fig. 18. RMS bending curvature differences with different sensor spacings.

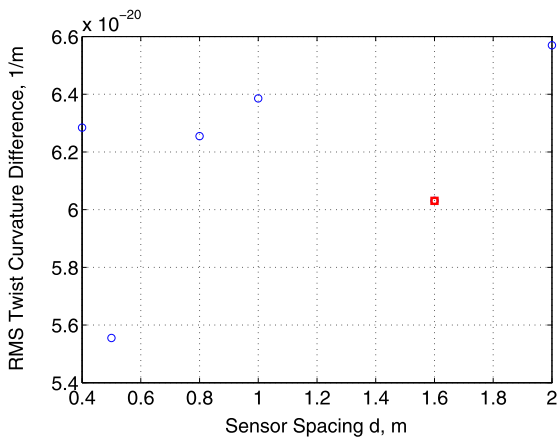


Fig. 19. RMS twist curvature difference with different sensor spacings.

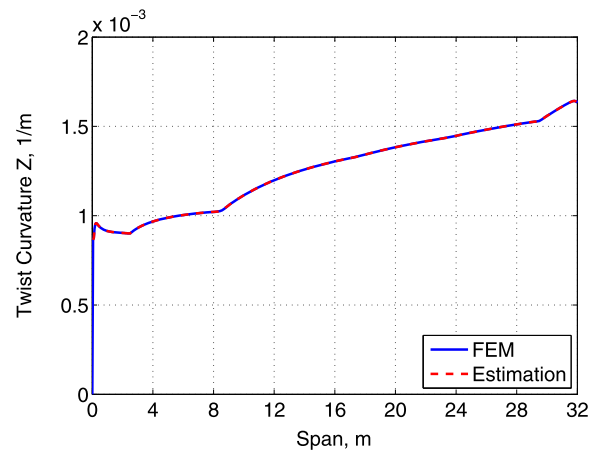


Fig. 21. Twist curvature about the z axis from FE simulation and Estimation.

formed with loads of different frequencies. Lateral loads of 100 kN are applied in both the  $x$  and  $y$  directions with a  $10.94 \times 10^6$  N-m torque applied about the  $z$  axis at the tip of the rocket. The tank pressures are the same as the previous cases, yet they are applied with a 1-s linear ramp to avoid the transient effects at the beginning of simulations. The loads are applied in three ways: one step input and two sinusoidal inputs with longer durations at 5 and 20 Hz, respectively (denoted as “Step”, “5 Hz”, and “20 Hz”). The simulations are performed for 5 s with  $\Delta t = 10$  ms for the first two cases and 2 s with  $\Delta t = 1$  ms for the last case. The step load

in the first case is applied between 1.10 and 1.15 s. The sinusoidal loads in the other two cases are applied from the time point that is 1.1 s after the tank pressures are fully ramped up.

Figs. 23 and 24 show the single-sided spectra of bending vibrations in the  $x$  and  $y$  directions and torsional vibration about the  $z$  axis at the 30-m span under different loads. According to Fig. 23, the dominant bending vibration of the notional rocket is at its natural frequency. Therefore, bending sensitivities for the curvature estimation are calibrated for the simulation of the rocket model

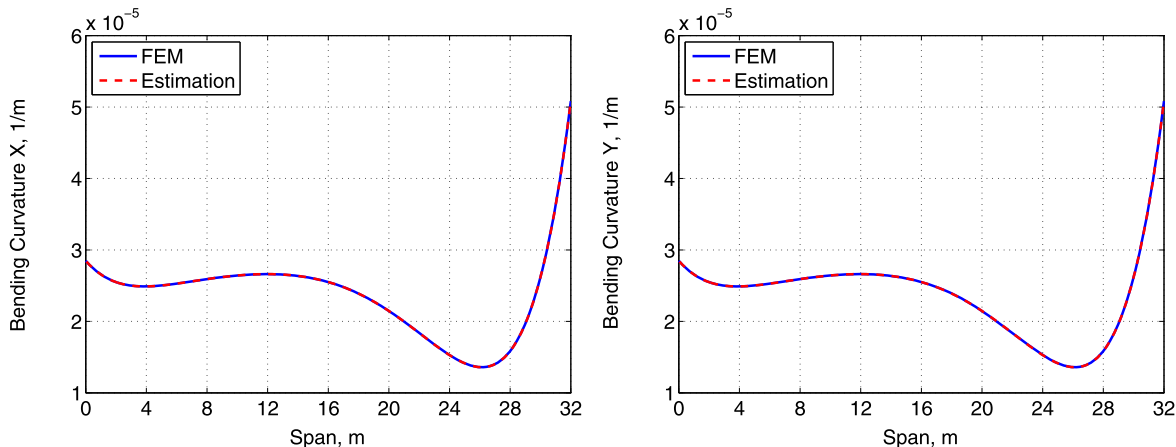


Fig. 20. Bending curvatures from FE simulation and estimation.

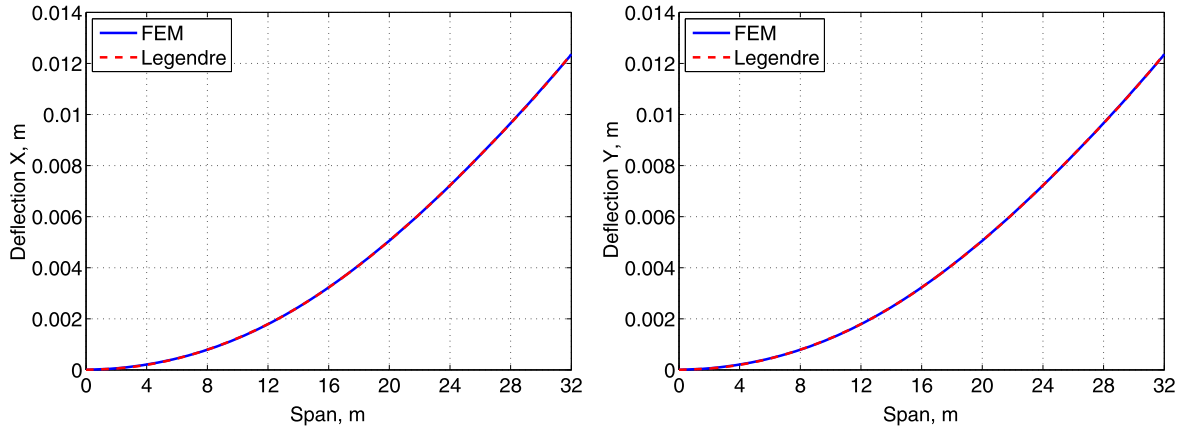


Fig. 22. Comparison between estimated deflections of rocket center axis and FE simulation results (first 22 Legendre polynomials used).

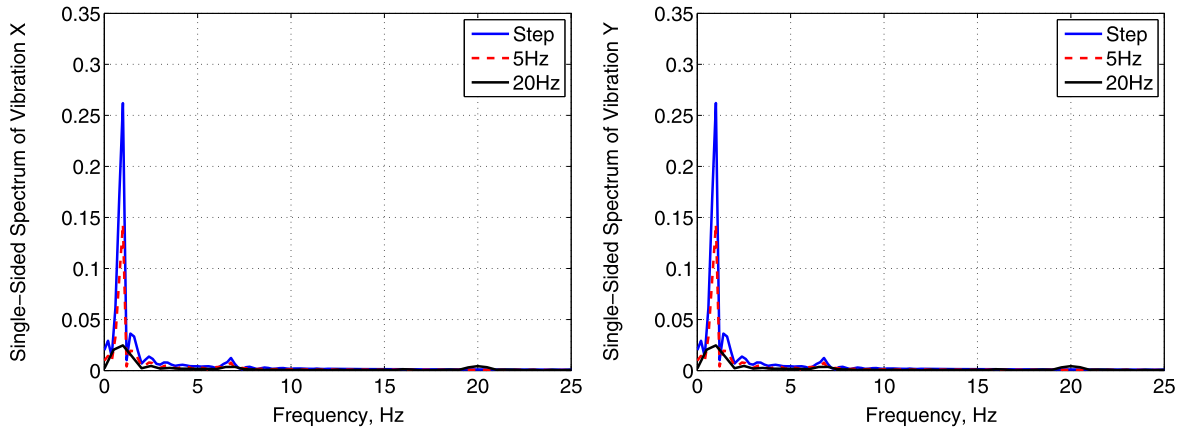


Fig. 23. Single-sided spectra of bending vibrations at the 30-m span.

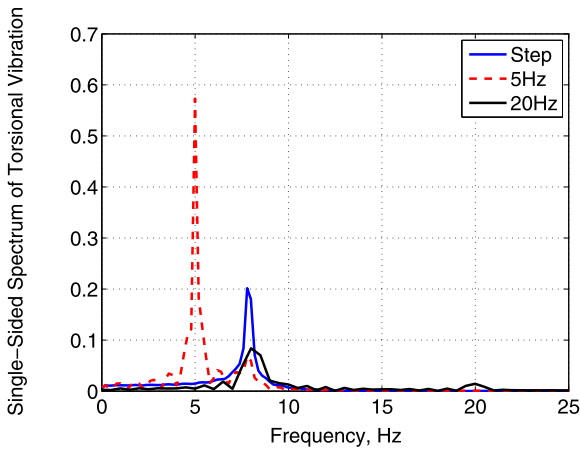


Fig. 24. Single-sided spectra of torsional vibration at the 30-m span.

with a step load input. On the other hand, the dominant torsional vibration of the rocket model in the cases are different based on excitations as shown in Fig. 24. Hence, it is better to calibrate the torsional sensitivity for the curvature estimation with respect to each excitation.

Figs. 25 and 26 show the bending deflections and twist curvature from FE simulations and estimations at  $t = 5$  s with the step tip load. According to Fig. 25, the estimation of bending captures the deflection shapes and magnitudes due to the instantaneous disturbance at the vehicle top accurately. The estimation of twist

curvature also captures the tendency of the deformation, yet the accuracy is relatively low compared to that of bending. The error close to the loading point (between span of 26 and 32 m in Fig. 26) is especially high. The bending deflections and twist curvature from FE simulations and estimations with the two sinusoidal tip loads at  $t = 5$  and 2 s, respectively, are plotted in Figs. 27 to 30. Fig. 27 shows that the bending deflections can be precisely predicted with the low-frequency vibration dominated by the first bending mode. The torsional deformation with the low-frequency excitation (see Fig. 28) is estimated accurately up to 24-m span, but the accuracy is degraded around the excitation point, the same as what was observed in Fig. 26. With the high-frequency tip excitation, the second bending mode plays a role in the vibrations as shown in Fig. 29. However, the bending estimation still remains accurate. On the other hand, the twist estimation with the high-frequency excitation exhibits the similar behavior to the previous cases.

To quantify the overall accuracy of the estimated deflections ( $u$  and  $v$  in the  $x$  and  $y$  directions) or twist curvature  $\kappa_z$ , one may calculate the RMS difference of these quantities at each time using the spanwise values from the FE simulation and estimation (similar to Eq. (13)). The “maximum error” is found by using the ratio between the maximum RMS difference and the maximum absolute value of the corresponding variable in the range of simulation time. For example, the maximum error the bending deflection in the  $x$  direction is

$$e = \frac{\left(\sqrt{\frac{1}{N} \sum_{n=1}^N (u^{FEM} - u^{EST})^2}\right)_{\max}}{(u^{FEM})_{\max}} \quad (15)$$

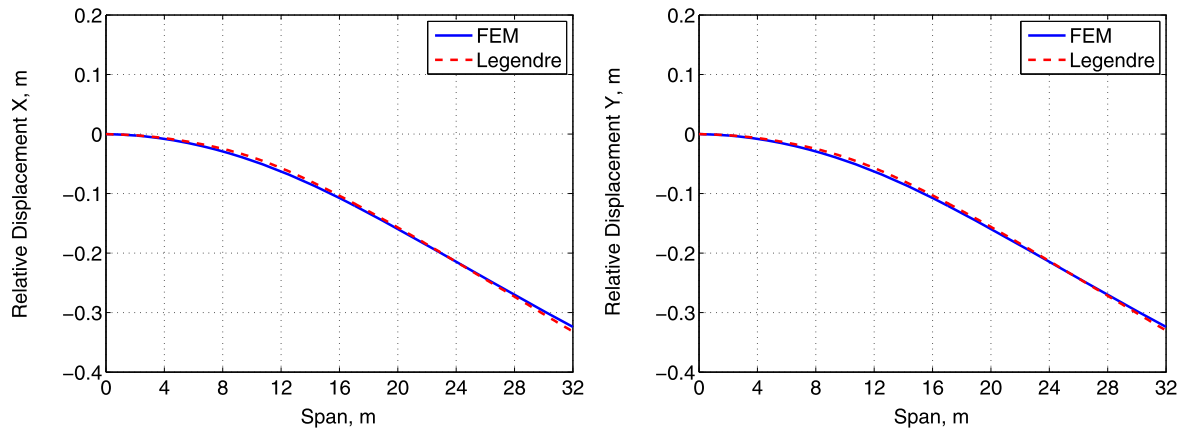


Fig. 25. FE simulation and estimation of deflections at 5 s with the step tip loads.

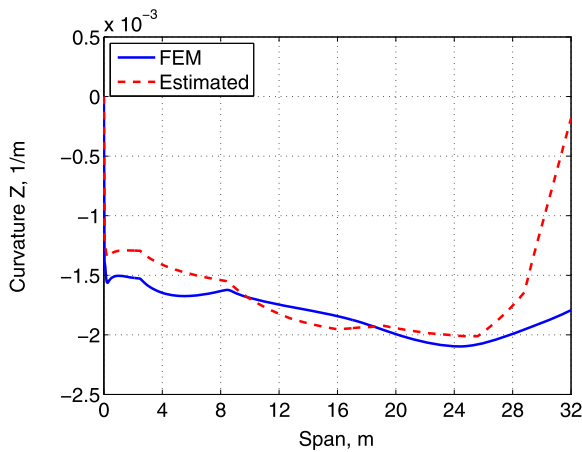


Fig. 26. FE simulation and estimation of twist curvature at 5 s with the step tip loads.

The estimation errors of other quantities are defined in a similar way. Following these definitions, Table 4 lists the maximum errors for the deflections and curvature. The results agree with the previous observations. The maximum error of bending deflections is less than 10%, which means the bending deflections are predicted with good accuracy at any time point and any spanwise location. The maximum error of twist curvature is high due to the discrepancies between the FE solutions and the estimations around the loading point (over span of 20 m). Based on the analysis, the estimations based on the RSS measurements can provide reasonably

accurate information about the rocket mode shapes and its magnitudes at any locations along the rocket at any time.

To ensure the validity of the sensitivities, other simulations with loads of different magnitudes and directions are performed. Table 5 shows the comparison of maximum errors with 5-Hz tip loads of different magnitudes and directions. It can be seen that the bending estimation is still very robust even with different load magnitude and direction.

## 5. Discussion

This study has demonstrated that with the combination of the strain sensors and reference strain structures, it can achieve cost-effective and reliable monitoring of shape/vibration of flexible rockets. In the optimization process of the RSS beams, one of the design constraints was that natural frequency of the RSS beams should be separated from those of the rocket, so that the RSS beams would not be excited by the vibration of the rocket. From the study, this design constraint was well satisfied. At this development phase, the number of sampling points used for the Kriging method was sufficient to demonstrate the concept of the surrogate-based optimization approach, which also provided feasible solution of the optimal design. It is preferable that a quality check of the Kriging surface would be performed, which might require more sampling points for the surface generation and validation. Additionally, one needs to be cautious when selecting the Legendre polynomials for approximation of mode shapes. Generally, higher order polynomials may cause inaccurate fitting results, as displayed in Ref. [9]. However, according to the current results, the inclusion of up to the 22nd-order Legendre polynomial still

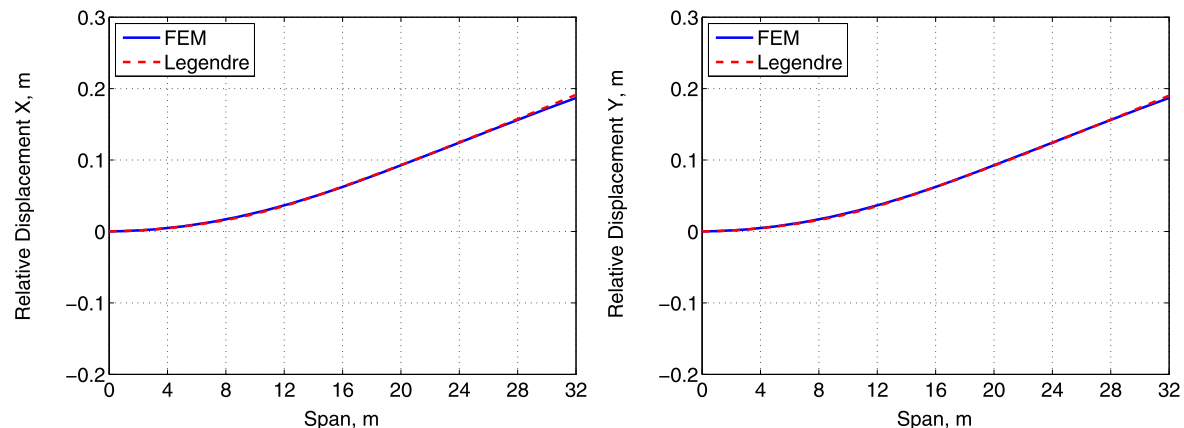


Fig. 27. FE simulation and estimation of deflections at 5 s under the 5-Hz sinusoidal tip loads.

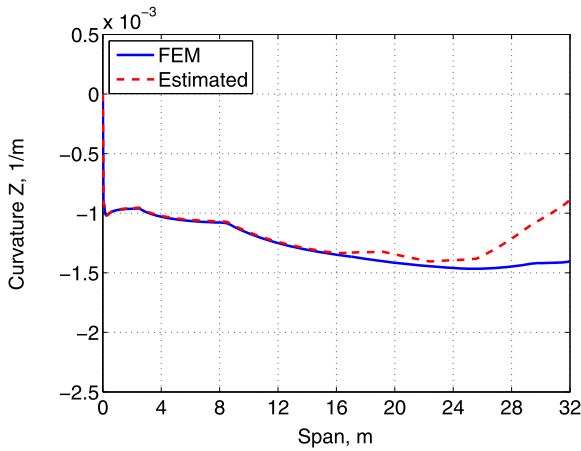


Fig. 28. FE simulation and estimation of twist curvature at 5 s under the 5-Hz sinusoidal tip loads.

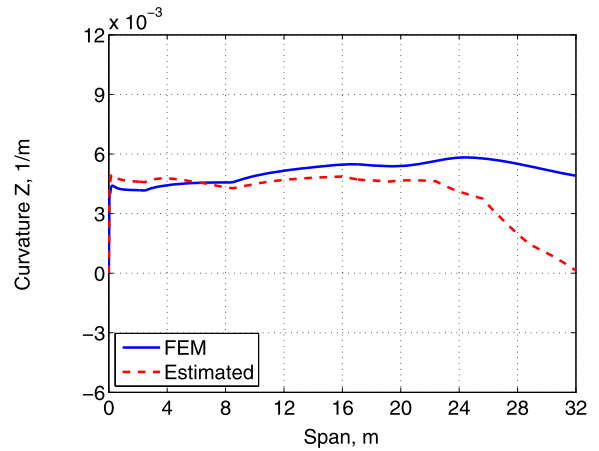


Fig. 30. FE simulation and estimation of twist curvature at 2 s under the 20-Hz sinusoidal tip loads.

provided good convergence and satisfactory robustness. The reason was that enough data (more than 640 points) along the span of rocket were used to approximate the mode shapes of the rocket. Note that the numeric studies of estimating the performance of RSS beams used the cantilever boundary condition with applied tip load excitations. Further studies that simulate launches of flexible rockets with engine excitation at the bottom will be performed in the future. Finally, as stated in the Introduction, this paper explored how the strain sensors and RSS structures work together with full-size flexible rockets. Therefore, the full-size rocket model with specific parameters were used in the RSS design and optimization. To make the study generic and applicable to different rockets, future work will consider structural scaling in the methodology, where dimensionless parameters can be used.

### 6. Conclusions

Multi-axial reference strain structures were studied in this paper to monitor the bending and torsional vibrations of flexible rockets. Three RSS beams with 120° angular spacing were attached on the surface of the rocket, where strain sensors were instrumented. Even though the use of RSS beams only provides indirect measurement of rocket deformations, this measurement approach has the advantages in cost and reliability. Kinematic equations were derived to estimate the multi-axial bending and torsional deformations of the rocket center axis, based on the measured strain data on its surface. To enable accurate estimation of such deformations, the strains measured by the sensors on the RSS beams

must be the same as those of the rocket surface. While a difference might exist in such an indirect measurement, the error was minimized by the optimally designed RSS beam structure and the placement of the strain sensors long them. A surrogate-based optimization algorithm was developed by integrating the Kriging method and NSGA-II. The optimization algorithm allowed for a simple integration with the finite element analysis with MSC.Nastran. From the two-step optimization process, one could find the optimum structure design of the RSS beams (including the parameters of the linkage spacing in the longitudinal direction  $l$ , the radial spacing  $r$ , RSS beam cross-sectional thickness  $h$ , and cross-sectional width  $b$ ), which featured the minimized error between the strains of the rocket surface and the corresponding RSS beams. In the current study, strain sensors were considered to be evenly placed along the RSS beams. The optimum sensor spacing is chosen by considering a balance between the data processing accuracy and the allowed channel of data collection. The optimized RSS structure and the sensor placement were then verified in transient simulations. The maximum error of bending deflections under the tip load with a cantilever boundary condition was less than 1.7% for the excitation with a step load. The errors of the forced vibration of 5 and 20 Hz sinusoidal excitations were 2.7% and 9.8%, respectively. The bending estimation was also accurate with different load magnitudes and directions. The estimation of torsional curvatures was accurate up to 20-m span, but relatively large errors were observed around the tip where the loads were applied.

This study has demonstrated the concept of monitoring the bending and torsional vibrations using reference strain structures.

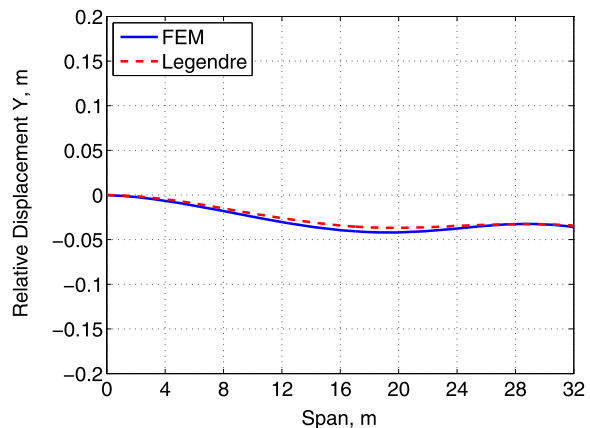
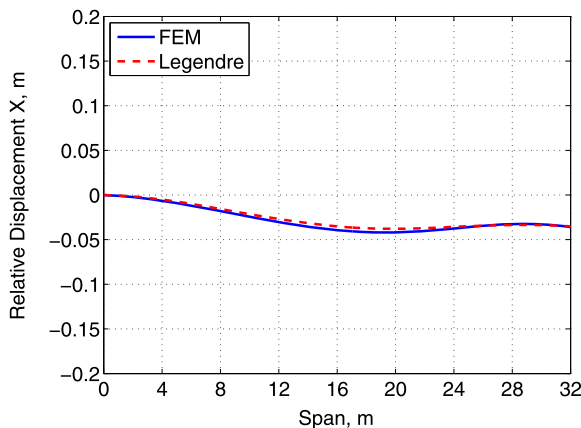


Fig. 29. FE simulation and estimation of deflections at 2 s under the 20-Hz sinusoidal tip loads.

**Table 4**

Ratios of maximum RMS differences to maximum deflections and curvatures with different excitations.

Excitation	Deflection in X (%)	Deflection in Y (%)	Curvature about Z (%)
Step load	1.70	1.47	21.40
Sinusoidal at 5 Hz	2.66	2.63	8.47
Sinusoidal at 20 Hz	7.95	9.76	52.52

**Table 5**

Ratios of maximum RMS differences to maximum deflections and curvatures under the tip loads at 5 Hz with different loading magnitudes and directions.

Magnitude scale	Direction (degree)	Deflection in X (%)	Deflection in Y (%)
1	45	2.66	2.63
10	45	2.77	2.75
1	60	2.83	2.75

The accuracy of the bending estimation, which is more important than torsion in attitude control of rockets, make it feasible to be used in control development of flexible rockets. The removable RSS beams provide the spanwise placement freedom of strain sensors. Furthermore, the maintenance of RSS beams (e.g., redesign and replacement) is convenient without interfering with the main structure of the rocket.

#### Conflict of interest statement

There is no conflict of interest.

#### Acknowledgements

This work was supported by the NASA Launch Service Program Special Studies (LSP-15-011 and LSP-15-032). The views expressed in this paper are those of the authors and do not reflect the official policy or position of NASA or the U.S. Government.

#### References

- [1] N.A. Bletsos, Launch vehicle guidance, navigation, and control, *Crosslink* 5 (2004) 30–33.
- [2] E.J. Friebele, C.G. Askins, G.A. Miller, J.R. Peele, L.R. Wasserman, Optical fiber sensors for spacecraft: applications and challenges, in: *Photonics for Space Environments IX*, in: SPIE, vol. 5554, International Society for Optics and Photonics, 2004, pp. 120–131.
- [3] R. Di Sante, Fibre optic sensors for structural health monitoring of aircraft composite structures: recent advances and applications, *Sensors* 15 (2015) 18666–18713.
- [4] M. Ramakrishnan, G. Rajan, Y. Semenova, G. Farrell, Overview of fiber optic sensor technologies for strain/temperature sensing applications in composite materials, *Sensors* 16 (2016).
- [5] M. Varasi, A. Vannucci, M. Signorazzi, P. Ferraro, S.I. Imperato, C. Voto, J.R. Dunphy, G. Meltz, Integrated optical instrumentation for the diagnostics of parts by embedded or surface attached optical sensors, U.S. Patent 5,493,390, 1996.
- [6] J.R. Dunphy, G. Meltz, M. Varasi, A. Vannucci, M. Signorazzi, P. Ferraro, S.I. Imperato, C. Voto, Embedded optical sensor capable of strain and temperature measurement using a single diffraction grating, U.S. Patent 5,399,854, 1995.
- [7] H.M. Chan, A.R. Parker, A. Piazza, W.L. Richards, Fiber-optic sensing system: overview, development and deployment in flight at NASA, in: *IEEE, Avionics and Vehicle Fiber-Optics and Photonics Conference, AVFOP, IEEE, Santa Barbara, CA, 2015*, pp. 71–73.
- [8] H. Gutierrez, B.S. Javani, D. Kirk, W. Su, M. Wolf, E. Griffin, Fiber optic sensor arrays for real-time virtual instrumentation and control of flexible structures, in: A. Wicks, C. Niezrecki (Eds.), *Structural Health Monitoring, Damage Detection & Mechatronics*, Springer International Publishing, Cham, Switzerland, 2016, pp. 9–22.
- [9] W. Su, C.K. King, S.R. Clark, E.D. Griffin, J.D. Suhey, M.G. Wolf, Dynamic beam solutions for real-time simulation and control development of flexible rockets, *J. Spacecr. Rockets* 54 (2017) 403–416.
- [10] G. Lapilli, Multi-Axial Fiber Optic Reference Strain Sensor for Flexible Dynamics of Structures, Ph.D. Diss, Florida Institute of Technology, Melbourne, FL, 2016.
- [11] R.P. Miller, T.F. Gerus, Experimental Lateral Bending Dynamics of the Atlas-Centaur-Surveyor Launch Vehicle, NASA TM-X-1937, 1969.
- [12] Lewis-Research-Center, Flight Performance of Atlas-Centaur AC-13, AC-14, AC-15 in Support of the Surveyor Lunar Landing Program, NASA-TM-X-1844, 1970.
- [13] Lewis-Research-Center, Atlas-Centaur AC-17 Performance for Applications Technology Satellite ATS-D Mission, NASA-TM-X-2525, E-6510 1972.
- [14] K. Deb, A. Pratap, S. Agarwal, T. Meyarivan, A fast and elitist multiobjective genetic algorithm: NSGA-II, *IEEE Trans. Evol. Comput.* 6 (2002) 182–197.
- [15] D.G. Krige, a statistical approach to some basic mine valuation problems on the Witwatersrand, *J. S. Afr. Inst. Min. Metall.* 94 (1994) 95–111.